Available online at www.sciencedirect.com
SCIENCE DIRECT®
Surface Science 561 (2004) 154–170
SURFACE SCIENCE
www.elsevier.com/locate/susc

Aspects of spin-polarized scanning tunneling microscopy at the atomic scale: experiment, theory, and simulation

Arthur R. Smith [a,*], Rong Yang [a], Haiqiang Yang [a], Walter R.L. Lambrecht [b], Alexey Dick [c,d], Joerg Neugebauer [c,d]

[a] *Condensed Matter and Surface Science Program, Department of Physics and Astronomy, Ohio University, Clippinger 251B, Athens, OH 45701, USA*
[b] *Department of Physics, Case Western Reserve University, Cleveland, OH 44106-7079, USA*
[c] *Theoretische Physik, Universität Paderborn, Warburger Str. 100, 33098 Paderborn, Germany*
[d] *Fritz-Haber-Institut der MPG, Faradayweg 4-6 D-14195 Berlin (Dahlem), Germany*

Received 25 August 2003; accepted for publication 10 May 2004
Available online 31 May 2004

Abstract

The principle and method of atomic-scale spin-polarized scanning tunneling microscopy is discussed, and its application to the case of the (0 1 0) surface of η-phase Mn_3N_2 is presented. For this surface, new proofs of the spin-polarized effect are presented, and it is also shown that the spin-polarized effect can turn on and off with small changes to the tip apex which can occur during scanning; this indicates that the tip magnetic density of states can and does change at certain points during the experiment. It is also shown how to model height profile data using spin-polarized local density of states of the sample. As well, it is shown how to relate the equation for the total spin-polarized height profile to those of the separated magnetic and non-magnetic height profiles. Comparison of the experimental height profiles to the simulated height profiles based on spin-polarized local densities of states calculated from first-principles density functional theory is shown. In particular, a comparison is made between the results of using the atom-superposition method vs. a full Tersoff–Hamman simulation method. For the case of the transition metal nitride system here, it is shown that the latter method is crucial for a full understanding due to the directionality of the atomic orbital lobes.

Keywords: Scanning tunneling microscopy; Nitrides; Magnetic surfaces

1. Introduction

Atomic-scale scanning tunneling microscopy (STM) is a well established technique for obtaining height or current maps of the local density of states (LDOS) of a sample surface [1–6]. Only recently it has been shown that, in addition to the usual non-magnetic or chemical information, atomic-scale STM can also obtain maps of the magnetic structure of a sample surface if a magnetized probe tip is used [7,8]. Part of the difficulty of establishing atomic-scale spin-polarized STM (SP-STM) as a reliable technique has been obtaining ideal,

* Corresponding author. Tel.: +1-740-5972576; fax: +1-740-5930433.
E-mail address: smitha2@ohio.edu (A.R. Smith).

0039-6028/$ - see front matter © 2004 Elsevier B.V. All rights reserved.
doi:10.1016/j.susc.2004.05.011

model surfaces with atomic-scale magnetic variations—i.e. an antiferromagnetic (aFM) surface. In one of the earliest reports of SP-STM, Wiesendanger et al. applied SP-STM to the surface of Cr(0 0 1) in which the spin moments are ferromagnetic (FM) within a terrace but reverse upon crossing a monolayer (ML) height step, showing that an alternation in the measured ML step heights was obtained [9]. The two measured ML step heights bracketed the one obtained using a non-magnetic tip, thus showing that the tip-sample distance for one terrace was larger than the tip-sample distance for the other terrace, since constant current (CC) mode was used. The result implies that *if* the tip-sample distance could be held constant for both terraces, then the tunneling current would be larger for one terrace than for the other. The tunneling current therefore is found to depend on the direction of the surface spin vectors relative to the tip spin vector. This principle can be applied to obtain magnetic contrast on a surface in which the spin vectors change direction, for example, from row to row as was shown by Heinze et al. for a Mn ML on W(1 1 0) [7]. But in addition, it should also be the case that both magnetic and non-magnetic information can be obtained, as we have shown in a recent Letter [8].

A theoretical explanation for the spin-sensitivity on an aFM surface has been given by Wortmann et al. and by Bode et al. [10,11]. Due to the importance of this method, there is need for further explanation and development of the theoretical modeling of atomic-scale SP-STM data; moreover, it is important to demonstrate the use of this method in the case of different magnetic surfaces since until our recent work [8], only Heinze et al. had demonstrated atomic-scale resolution in SP-STM imaging [of a Mn ML on W(1 1 0)] [7]. In this work, we provide additional confirmations and proofs of the theory and application of atomic-scale SP-STM in the case of the surface Mn_3N_2(0 1 0). First, we present images illustrating the on–off behavior of the SP effect, showing that the observed magnetic row height modulation is a function only of the polarization of the STM tip. Second, we present SP-STM data in the vicinity of two different types of step edges, showing that the step edge has no effect on the observed magnetic modulation, which is due simply to the fact that the surface magnetic structure is directly related to the bulk magnetic structure in the case of Mn_3N_2(0 1 0). Third, the theoretical modeling of the SP-STM height profile is developed, and the separated equations for the magnetic and non-magnetic height profiles are obtained from the total SP-STM height profile equation in terms of the majority and minority LDOS. Fourth, density functional theory (DFT) is applied to Mn_3N_2(0 1 0), obtaining the LDOS vs. energy and surface LDOS maps. Simulated height profiles based on both atom superposition model and DFT surface LDOS calculations are performed and compared with those from experiment in the case of Mn_3N_2(0 1 0). The results conclusively demonstrate atomic-scale SP-STM as a powerful tool to obtain magnetic contrast at ultra-small (atomic) length scales.

2. Experiment

The experiments are performed in a custom-designed ultra-high vacuum system consisting of a MBE chamber coupled to a surface analysis chamber where the STM system is located, which allow us to study the surfaces of grown films in situ. The MBE system includes a solid source effusion cell for Mn, an e-beam cell for Fe, and a RF plasma source for N. After being heated up to 1000 °C for 30 min with the nitrogen plasma turned on, the MgO substrate temperature is lowered to the growth temperature (at this stage, the reflection high energy electron diffraction (RHEED) pattern of MgO is streaky, indicating the substrate is smooth after treatment), and the growth begins. The growth condition is monitored using RHEED which enables the determination of the surface crystal symmetry and surface lattice parameters. The RHEED pattern of the film is streaky, indicating epitaxial growth [12,13].

Following growth, the samples are investigated with in situ STM and SP-STM. For normal STM studies, we use electrochemically etched tungsten tips which are cleaned in the ultra-high vacuum chamber using electron bombardment. For these SP-STM studies, we coat the cleaned tips with Mn, MnN, or Fe at room temperature to a thickness of several monolayers. MnN is aFM in bulk with

$T_{Néel} \sim 650$ K [14–16]. While the Néel temperature of bulk Mn is only ~100 K [17], spin-polarized photoelectron diffraction of thin films of Mn have shown spin asymmetry up to ~500 K, which was attributed to the surface atoms [18]. In the case of Fe (T_c of Fe is 1043 K) coatings, the tips are subsequently placed in a magnetic field (about 40 mT) with the field direction normal to the tip axis. All STM and SP-STM imaging is performed at ambient temperature (300 K) in constant current (CC) mode.

3. Results and discussion

3.1. SP-STM imaging of $Mn_3N_2(0\,1\,0)$

3.1.1. Magnetic tip switching during STM imaging using aFM-coated tips

Shown in Fig. 1 are successive STM images of $Mn_3N_2(0\,1\,0)$ obtained using a MnN-coated W tip. Both images were acquired on the same surface area (which is clear from the defect and the step edges) and at the same sample bias $V_s = -0.4$ V and the same tunneling current of 0.5 nA. No spin-polarized effect is observed in Fig. 1(a), whereas a clear spin-polarized effect is observed in Fig. 1(b). The normal image in Fig. 1(a) looks exactly like other normal STM images obtained with a normal W tip [8,12]. The spacing of the rows is 6.07 Å, corresponding to the spacing between rows without nitrogen in the $Mn_3N_2(0\,1\,0)$ surface model [Fig. 1(c)]. In Fig. 1(b), the row heights appear modulated, with every other row appearing higher. The spacing of the high rows is 12.14 Å, double the row spacing in Fig. 1(a), and corresponds to the magnetic period of the Mn_3N_2 (0 1 0) surface which equals c. The spin direction of the Mn atoms in the rows without N repeats with period $= c$.

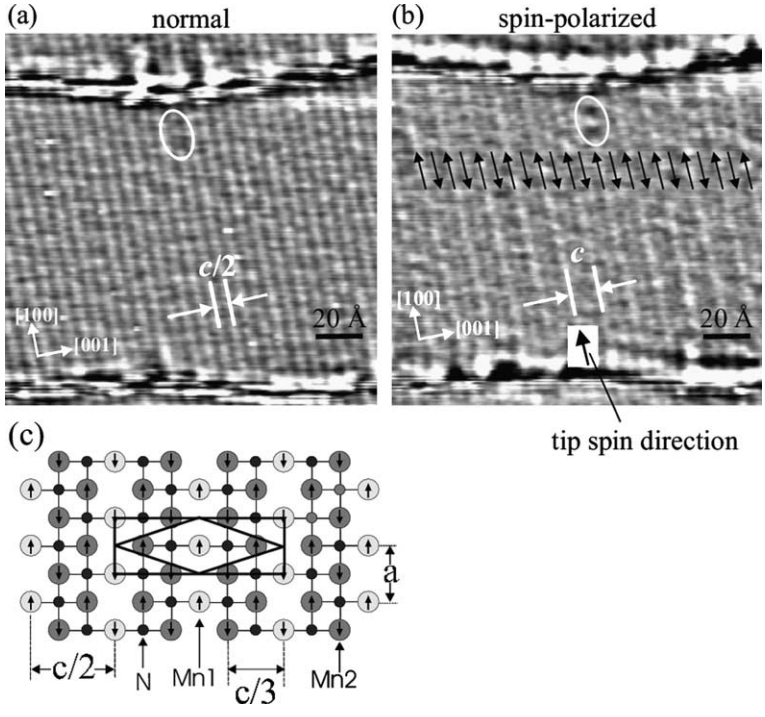

Fig. 1. Sequential STM images of the same surface area obtained using a MnN-coated W tip showing normal image (a)and spin-polarized image (b). Both (a) and (b) were obtained at a sample bias $V_s = -0.4$ V and a tunneling current $I_t = 0.5$ nA. The ellipses mark the same point defects in the images. The arrows in (b) indicate the orientations of spin in the rows while the separated arrow indicates the orientation of the tip spin. A local background subtraction has been applied to the data. Shown in (c) is a surface model of $Mn_3N_2(0\,1\,0)$.

To understand better the origin of the height modulation, the model of the $Mn_3N_2(0\,1\,0)$ surface must be considered. In the bulk-like model of the surface shown in Fig. 1(c), it is seen that there are Mn atoms in two types of bonding configurations on the surface which are referred to as Mn1 and Mn2. Mn1 atoms have 2 surface N neighbors, while Mn2 atoms have 3 surface N neighbors and 1 subsurface N neighbor. While Mn1 and Mn2 atoms each have spin, the direction of spin alternates from row to row. The spins are ferromagnetic within a row but antiferromagnetic from row to row along the c-direction. The surface magnetic structure coincides with the bulk magnetic structure [16,19,20,32]. The row height modulation is due to the spin-polarized effect: when the spin of the tip is parallel to the spin of the surface atom, the tunneling current is larger; when the tip spin is antiparallel to the spin of the sample, the tunneling current is smaller [8]. The modulation with period c corresponds to the magnetic period at the surface.

Modulation having shorter period of $c/3$ is not observed in Fig. 1(b). While a sharper tip might be able to observe finer magnetic structure at certain voltages, the present result shows that the larger magnetic period $= c$ is dominant. A general explanation for this behavior, for example that larger real-space periods should be dominant in STM images, has been given elsewhere [7]. However, sharper STM tips do allow to obtain the atomic-resolution images of the $Mn_3N_2(0\,1\,0)$ surface showing the individual Mn1 and Mn2 atoms [8,21]. At certain bias voltages, the magnetic data does contain more detailed information as well, given a sharp tip.

The change of the magnetic state of the tip between Fig. 1(a) and (b) is evidently due to atom rearrangements at the tip apex. Tip-sample interactions are well known to cause changes in the performance of STM tips in normal STM, and these interactions are currently being exploited in order to achieve atom and molecule manipulation on surfaces [22–24]. The STM tip can interact with a surface to pick up or drop some atoms during a normal line scan. Recently, Yamada et al. have shown that voltage pulses can be used to turn a plain W tip into a magnetic-coated W tip when the surface is Mn(0 0 1) on Fe(0 0 1) whiskers [25]. In the case presented here, the tip was already coated with MnN which is aFM in bulk, and the surface is Mn_3N_2; since no tip pulsing was used in this case, we find that the state of the tip can even change without using tip pulsing. Note that tip changes in normal STM also commonly occur during the course of scanning. Of course tip pulsing may also be used to change the state of the tip, which is another common technique to modify the performance of even normal STM tips. These results therefore prove that only small changes to the state of the tip can change a magnetic tip to be a non-magnetic tip or vice versa. Therefore, it shows that the spin-polarized effect is caused by only the one atom or a few atoms at the tip apex. Of course the tip atom or atoms may be coupled to a larger magnetic reservoir, which may provide stability to the tip atom's spin orientation. Also, given that the tip atom–atom distance is typically 2–3 Å, whereas the tip atom-sample atom distance is typically 3–7 Å for atomic-scale STM [26], then the tip atom-tip atom magnetic interaction is clearly stronger than the tip atom-sample atom magnetic interaction anyway, just as in normal STM.

3.1.2. SP-STM in vicinity of step edges on Mn_3N_2 (0 1 0)

Fig. 2(a) and (c) show SP-STM images obtained using Mn-coated W tip showing two types of step edges. The images are displayed using a local background subtraction which results in an artificial brightening at the step edges but which shows contrast on all the terraces. In Fig. 2(a) is an SP-STM image showing the atomic rows crossing approximately perpendicular to the step edges, which we call Type I step edges; this image was acquired at sample bias $V_s = -0.4$ V and tunneling current $I_t = 0.8$ nA. A model of the type I step edge is shown in Fig. 2(b). The height modulation of the rows which run along [1 0 0] is clearly evident on all 3 terraces. We note that the higher rows on one terrace are continued across the step edge onto the next terrace without any shift along the step edge direction, as is indicated by the black/white dashed lines crossing the steps. While the tip spin vector does not change throughout the whole image, the sample spin directions within a [1 0 0]

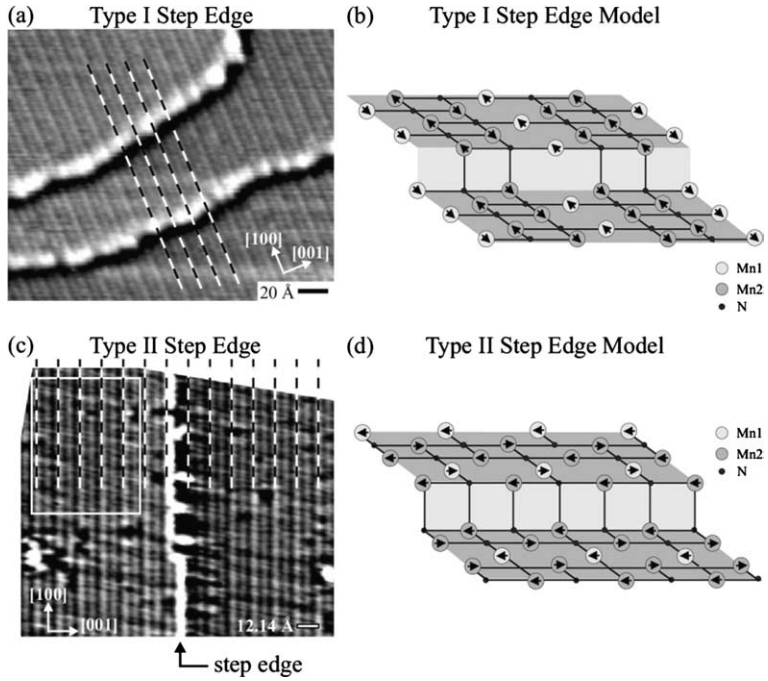

Fig. 2. (a) Spin-polarized STM image obtained at a sample bias $V_s = -0.4$ V and a tunneling current $I_t = 0.8$ nA using Mn-coated W tip. Dashed lines indicate positions of the high magnetic peaks across the step edge without shift. Enhancement at step edge is due to a local background subtraction. (b) Step edge model for the case where [1 0 0] rows are $\perp$ to the step edge. (c) SP-STM image obtained at a sample bias of $V_s = -0.2$ V and a tunneling current $I_t = 0.3$ nA. (d) Step edge model for the case where [1 0 0] rows are parallel to the step edge.

row are constant as the row crosses the step edge, as seen clearly in the model of Fig. 2(b). This is due to the fact that the spin directions on the (0 1 0) surface are determined by the spin directions of the Mn atoms within ferromagnetic (0 0 1) bulk planes which intersect the surface at 90° to (0 1 0). Thus we should not expect any shift of the magnetic modulation across the Type I step edge, and none is seen. This result is additional proof of the spin-polarized effect on this surface.

Shown in Fig. 2(c) is a SP-STM image of a type II step edge in which the [1 0 0] rows are parallel to the step edge; this image was acquired using sample bias $V_s = -0.2$ V and tunneling current $I_t = 0.3$ nA. Clearly, the type II step edge is straighter than the type I step edge, suggesting that adatom diffusion is faster along the Type II step edge compared to the Type I step edge. The equally spaced black/white dashed lines corresponding to the high rows in the STM image show that the registry of the high rows is continued across the Type II step edge. This should be the case since the high rows of the SP-STM image correspond to the surface spin structure which in turn corresponds directly to the bulk spin structure. The corresponding Type II step edge model is shown in Fig. 2(d). In this model, the [1 0 0] atomic rows are parallel to the step edge, and we assume that the Mn2 atoms will compose the step edge atoms for greater stability. Shown in the model is just a single [1 0 0] row of Mn2 atoms at the step edge, although another model could be formed containing the double row of Mn2 atoms at the step edge. A lowest energy step edge model would require theoretical calculations.

3.1.3. aFM tip coatings for obtaining atomic-scale SP-STM images

The results presented in Figs. 1 and 2 also prove that it is not necessary to use FM-coated probe

tips to obtain atomic-scale SP-STM images. Heinze et al. demonstrated that FM-coated tips (W tips coated with either Fe or Gd) could produce atomic-scale SP-STM images of an aFM monolayer of Mn on W(1 1 0) [7]. Also, Kubetzka et al. have shown that aFM Cr-coated W probe tips could produce SP-STM images of two ML of Fe on W(1 1 0), obtaining resolution of FM stripe domains having magnetic period of 50 ± 5 nm [27]. One advantage of aFM-coated tips is that the vanishing tip stray field will allow to avoid the disturbance of the sample spin structure by the tip. The results shown here demonstrate that MnN and also Mn, which in bulk are aFM, can be used as tip coatings for the measurement of *atomic-scale* aFM structures.

3.1.4. Line profile analysis of atomic-scale SP-STM images

In the case of row-wise antiferromagnets such as $Mn_3N_2(0\,1\,0)$, in order to increase signal to noise in the experimental result, it is useful to take an average of the experimental line profiles along the direction of the rows ([1 0 0]). Shown in Fig. 3(a) is the STM image corresponding to the boxed region of the image of Fig. 2(c) which was acquired at $V_s = -0.2$ V and tunneling current of 0.3 nA. Shown in Fig. 3(b) is an averaged line profile corresponding to the STM image of Fig. 3(a). It is seen that the line profile displays the clear magnetic modulation of the peaks, which are spaced by $c/2$. The peak modulation is about 0.04 Å, while the total corrugation is ~0.13 Å. We also note a valley modulation of about 0.03 Å (vertical height modulations have estimated errors of ±0.01 Å). While fairly common, the valley modulation is not found in all sets of experimental data and therefore is an effect which depends on the tip. This effect is discussed further below. The total magnetic modulation period is just c, in accordance with the bulk-terminated surface magnetic period [see Fig. 1(c)].

The magnetic and non-magnetic components of the data are extracted from the total line profile by simply taking sums and differences of the two STM data height profiles $z(x)$ and $z(x+\frac{c}{2})$, as we have described in detail elsewhere [8]. Thus the

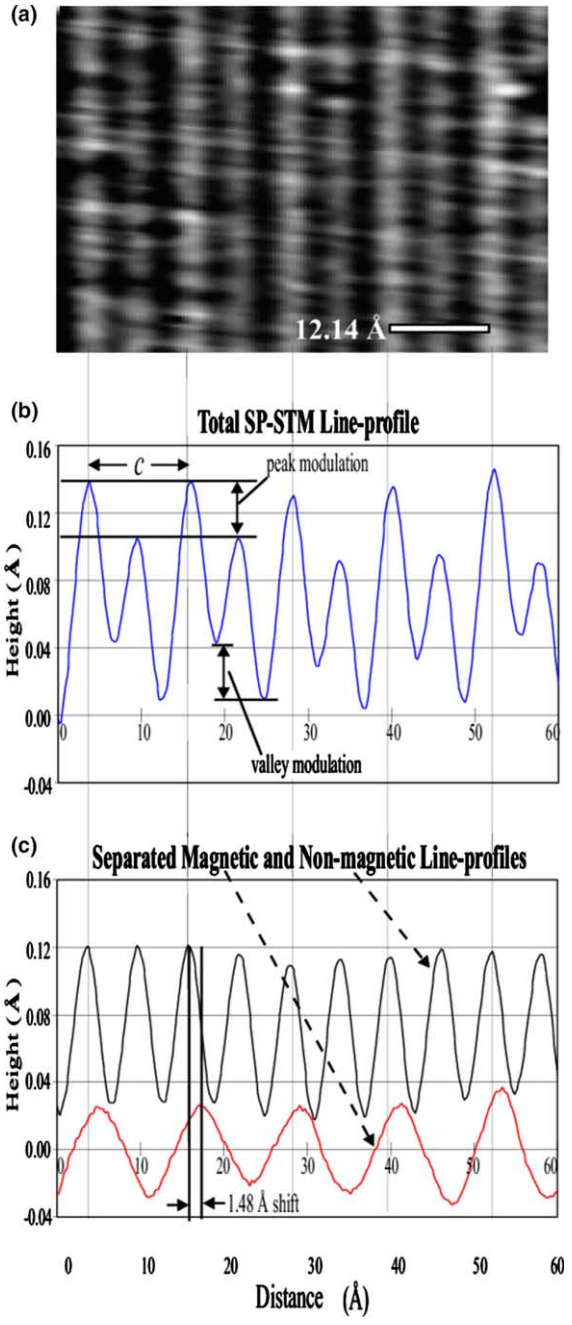

Fig. 3. (a) SP-STM image corresponding to the boxed region of Fig. 2(c), $V_s = -0.2$ V, $I_t = 0.3$ nA, Mn-coated W tip; (b) total SP-STM height profile averaged along [1 0 0]; (c) separated magnetic and non-magnetic height profiles.

deduced magnetic and non-magnetic height profiles corresponding to the total profile shown in

Fig. 3(b) are displayed in Fig. 3(c). It is seen that the non-magnetic component has a simple sinusoid-like form with period $\frac{c}{2}$. The amplitude of the non-magnetic peaks are all about the same. The non-magnetic peaks line up very closely with the peaks of the total profile (only a faint relative shift). The magnetic component also has an approximately sinusoidal form with a period c equal to twice the period of the non-magnetic component. The magnetic peaks have a fairly uniform amplitude and are shifted to the right relative to the non-magnetic component by $\sim$1.5 Å. This shift is responsible for the valley modulation seen in the total height profile [Fig. 3(b)]. Such shifts are fairly common; yet, some data show very little, or no, shift.

The peak shift is attributed to a kind of tip asymmetry in which the spatial centroid of the tip LDOS is not exactly coincident with the spatial centroid of the tip magnetic LDOS. To appreciate this, one need only think of an aFM tip where the outermost few tip atoms may have opposite spin directions. Suppose the outermost atom of the tip has a spin direction making a larger angle with the spin direction of the surface atom, while the next atom, slightly farther removed from the surface has a more collinear spin orientation with the surface atom directly below the tip. In that case, the total ILDOS would peak and give the strongest current contribution for the outermost tip atom, but the magnetic ILDOS would give the strongest current contribution from the next atom in the tip. These could easily be displaced by 1.5 Å. Magnetic contrast appears to work better with slightly rounded tips, and thus several atoms are expected to contribute, but it is in general not clear that all these tip surface atoms have exactly the same spin direction or are uniformly covering the surface of the tip. Thus we expect that the magnetic LDOS and total LDOS of the tip could be slightly displaced from each other. It should be kept in mind also that the profile results from an averaging of contributions from several surface atoms, and for the simulations, one may need in fact to take into account multiple tip atom contributions.

The data shown in Figs. 2 and 3 were acquired using a Mn-coated W tip, and the results indicate that the magnetic line profile is shifted compared to the non-magnetic line profile due to the apparent existence of a somewhat rounded tip. Shown in Fig. 4(a) is a STM image of the $Mn_3N_2(0\,1\,0)$ acquired using a Fe-coated W tip at the same bias voltage of $V_s = -0.2$ V. The magnetic modulation is clear in the image and is also clear in the average line profile shown in Fig. 4(b). Application of the separation procedure obtains the non-magnetic and magnetic components, as shown in Fig. 4(c), where it is noticed that the non-magnetic profile has a simple sinusoidal shape. However, the magnetic profile displays a slightly trapezoidal shape. Moreover, the magnetic component is not shifted as is the case with the data of Fig. 3. We interpret the difference in line profile shape to be due to a somewhat sharper tip, which is more symmetrical. We have previously reported this trapezoidal magnetic profile shape at −0.4 and −0.6 V using Fe-coated and Mn-coated W tips, respectively. Therefore, either Mn or Fe coatings can result in that shape, depending on tip sharpness.

3.2. Spin-polarized STM theory

The theory of atomic-scale SP-STM has been discussed by Wortmann et al. and by Bode et al. [10,11]. In the following, it is shown how the tunneling current in terms of up and down spin channels can be rewritten in terms of magnetic and non-magnetic channels.

3.2.1. STM tunneling current: ↑ and ↓ spin channels

First, we consider that in SP-STM, both spin-up (spin-↑) and spin-down (spin-↓) channels will contribute to the total tunneling current [10]. The LDOS of sample and tip are divided into two components each: $n_\uparrow^s$ and $n_\downarrow^s$ for the sample, and $n_\uparrow^t$ and $n_\downarrow^t$ for the tip. The tunneling current above a given surface location R_T is going to have the following form:

$$I_t \sim \int g_V(E)[n_\uparrow^t(E - eV_s)n_\uparrow^s(\vec{R}_t, E) + n_\downarrow^t(E - eV_s)n_\downarrow^s(\vec{R}_t, E)]\mathrm{d}E \quad (1)$$

where E_F is the Fermi level of the sample, $g_V(E) = f(E - E_F) - f(E - E_F - eV_s)$ where f is

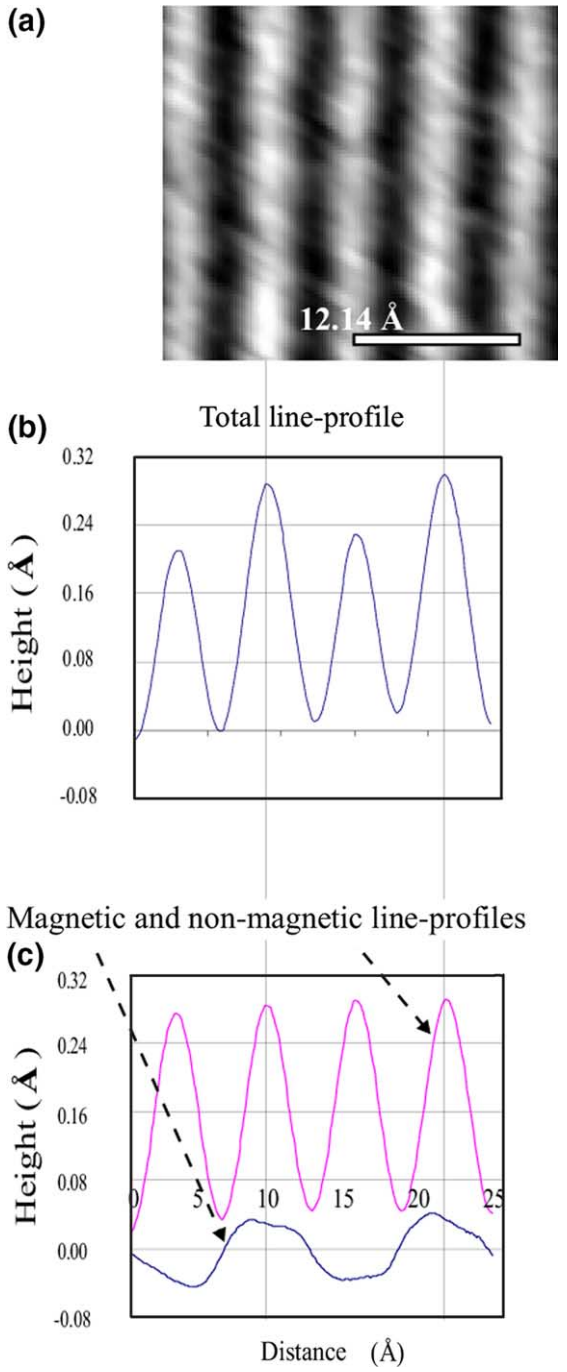

Fig. 4. (a) SP-STM image acquired at $V_s = -0.2$ V, $I_t = 0.8$ nA, Fe-coated W tip; (b) total SP-STM height profile averaged along [1 0 0]; (c) separated magnetic and non-magnetic height profiles.

the Fermi function, and $n^s_{\uparrow,\downarrow}(\vec{R}_t, E)$ is the spin-↑, spin-↓ LDOS of the sample at energy E and tip position $\vec{R}_t$. From Eq. (1) it is clear that the tunneling current is the sum of the convolution of the spin-↑ LDOS of sample and tip plus the convolution of the spin-↓ LDOS of sample and tip.

We shall denote the tip spin-↑ to be the majority spin ($n^t_\uparrow = n^t_>$) and the tip spin-↓ to be the minority spin ($n^t_\downarrow = n^t_<$). In the case where the sample spin-↑ is also majority and sample spin-↓ is also minority (tip and sample spin alignment), the tunneling current will be maximum, donoted $I_{t,max}$. In the case where the sample spin-↑ is minority and sample spin-↓ is majority (tip and sample spin anti-alignment), the tunneling current will be minimum, denoted $I_{t,min}$. Thus we have for these two cases:

$$I_{t,max} \sim \int g_V(E)[n^t_> n^s_> + n^t_< n^s_<]\mathrm{d}E \tag{2}$$

and

$$I_{t,min} \sim \int g_V(E)[n^t_> n^s_< + n^t_< n^s_>]\mathrm{d}E. \tag{3}$$

In Eqs. (2) and (3), the energy, tip position, and convolution dependencies, written explicitly in Eq. (1), are understood. In the case of a sample in which rows of atoms alternate in their majority and minority spin states (i.e. an antiferromagnet), the tunneling current is modulated as the tip scans across the rows in constant height (CH) mode, and the height of the tip will be modulated as the tip scans across the rows in the case of constant current (CC) mode. The CC modulation is seen in Figs. 1 and 2 in the case of $Mn_3N_2(0\,1\,0)$.

3.2.2. Separating the tunneling current into magnetic and non-magnetic components

From Eqs. (1)–(3), it is difficult to see how to separate the magnetic from the non-magnetic information contained within the STM line profiles, although the current clearly contains both kinds of information. However, it is possible to rearrange the equations in order to separate the magnetic and non-magnetic information, as follows. For the tip and sample spin alignment case,

$$I_{t,max} \sim \int g_V(E)\{n^t_> n^s_< + n^t_>(n^s_> - n^s_<) + n^t_< n^s_< + [n^t_<(n^s_> - n^s_<) - n^t_<(n^s_> - n^s_<)]\}\mathrm{d}E \tag{4}$$

$$\sim \int g_V(E)\{[n^t_> n^s_< + n^t_< n^s_>] + (n^t_> - n^t_<)(n^s_> - n^s_<)\}\mathrm{d}E \quad (5)$$

$$\sim I_{t,\min} + \int g_V(E)(n^t_> - n^t_<)(n^s_> - n^s_<)\mathrm{d}E \quad (6)$$

Thus the maximum current $I_{t,max}$ can be seen as the minimum current $I_{t,min}$+a magnetic component. If the tip is not spin-polarized ($n^t_> = n^t_<$) and/or the sample is not spin-polarized ($n^s_> = n^s_<$), then the minimum current $I_{t,min}$ will be observed in the experiment.

If the magnetic part is divided into two equal parts, a further simplification results:

$$I_{t,\max} \sim \int g_V(E)\left\{[n^t_> n^s_< + n^t_< n^s_>] + \frac{1}{2}(n^t_> - n^t_<)(n^s_> - n^s_<) + \frac{1}{2}(n^t_> - n^t_<)(n^s_> - n^s_<)\right\}\mathrm{d}E \quad (7)$$

$$\sim \int g_V(E)\left\{\frac{1}{2}[n^t_> n^s_< + n^t_< n^s_> + n^t_> n^s_> + n^t_< n^s_<] + \frac{1}{2}(n^t_> - n^t_<)(n^s_> - n^s_<)\right\}\mathrm{d}E \quad (8)$$

Thus we get for the maximum current case (tip and sample spin alignment) an equation for tunneling current involving the sums and differences of the majority and minority spin-polarized LDOS of sample and tip:

$$I_{t,\max} \sim \int g_V(E)\frac{1}{2}[(n^t_> + n^t_<)(n^s_> + n^s_<) + (n^t_> - n^t_<)(n^s_> - n^s_<)]\mathrm{d}E \quad (9)$$

Similarly, we get for the minimum current case (tip and sample spin anti-alignment):

$$I_{t,\min} \sim \int g_V(E)\frac{1}{2}[(n^t_> + n^t_<)(n^s_> + n^s_<) - (n^t_> - n^t_<)(n^s_> - n^s_<)]\mathrm{d}E \quad (10)$$

If we now define the (total) LDOS as $n^t = n^t_> + n^t_<$ and $n^s = n^s_> + n^s_<$, and the magnetic LDOS as $m^t = n^t_> - n^t_<$ and $m^s = n^s_> - n^s_<$, Eqs. (9) and (10) are seen as the 0° and 180° limits of the more general expression for the spin-polarized tunneling current, similar to that given by Wortmann: [10]

$$I_t \sim \int g_V(E)\frac{1}{2}[n^t n^s + m^t m^s \cos\theta]\mathrm{d}E \quad (11)$$

where θ is the angle between tip magnetic LDOS $\mathbf{m}^t$ and sample magnetic LDOS $\mathbf{m}^s$($m^t = |\mathbf{m}^t|$ and $m^s = |\mathbf{m}^s|$).

3.3. Spin-polarized STM simulations

Here we discuss the two separate approaches which may be taken in order to simulate SP-STM height profile data: (1) model the total (magnetic + normal) height profile; and (2) model the separated magnetic and normal height profiles. Methods 1 and 2 can each be performed using either the full Tersoff–Hamman method or an atom superposition model. We note that atom superposition methods have been applied by Tersoff and Hamman to simple metals such as Au(1 1 0) [1] and by Tromp et al. to Si(111) 7×7 [28]. However, it is not clear how successful this simple method may be in the case of SP-STM. Here we present the application of both approaches to the case of Mn_3N_2(0 1 0), showing that the atom superposition model, while obtaining a good agreement with the magnetic profile, results in a qualitative disagreement with the total profile. On the other hand, the full T–H calculation is in overall good qualitative agreement with the STM data. The limitation of the superposition approach is attributed to the fact that it does not take into account the directionality of the *spin-resolved* orbital lobes involved in transition metal nitride surfaces.

3.3.1. Atom superposition simulations

Both CH and CC atom superposition simulations based on Eq. (1) can be performed using the $n^s_\uparrow$ and the $n^s_\downarrow$ densities of states of the sample. To make an atom superposition simulation (either CH or CC) of the total STM line profile, the following summation over surface atoms is performed, where it is assumed that the ILDOS from each local atom of the surface contributes to the tunneling current of the STM tip at position $\vec{R}_t$ via an exponential decay factor:

$$I_t \sim \sum \int dE g_V(E)[n_\uparrow^t n_\uparrow^s(\mathbf{R}_i) + n_\downarrow^t n_\downarrow^s(\mathbf{R}_i)]e^{-2\kappa|\mathbf{R}_t-\mathbf{R}_i|}. \quad (12)$$

Since we have no knowledge about the energetic dependencies of $n_\uparrow^t$ and $n_\downarrow^t$, it is common to assume they are constant over the energy range of integration and thus to take them outside the energy integral. Values of $n_\uparrow^s$ and $n_\downarrow^s$ must be obtained from theory.

Alternatively, we may also perform the total STM line profile simulation, in the atom superposition method, using values of n^s and m^s as in Eq. (11). In this case, and assuming the magnetic and non-magnetic LDOS of the tip to be energy independent, the simulation equation becomes:

$$I_t \sim \sum \frac{1}{2} n^t \int dE g_V(E)[n^s(\mathbf{R}_i, E) + P_i^t m^s(\mathbf{R}_i, E)]e^{-2\kappa|\mathbf{R}_t-\mathbf{R}_i|}. \quad (13)$$

where $P_i^t = \frac{m^t}{n^t}\cos\theta_i$ is the effective spin polarization of the tip for the ith surface atom. Since the exact geometry, density of states, and magnetization of the tip are unknown and cannot be measured by experiment, P_i^t is taken as a parameter which is determined by comparing experimental and theoretical corrugation amplitudes.

Furthermore, it is possible to perform atom superposition simulations of both the normal (non-magnetic) and spin-polarized (magnetic) components of the tunneling current, using the following equations:

$$I_{t,\text{normal}} \sim \sum \frac{1}{2} n^t \int g_V(E) n^s(\mathbf{R}_i, E) e^{-2\kappa|\mathbf{R}_t-\mathbf{R}_i|} dE \quad (14)$$

$$I_{t,\text{magnetic}} \sim \sum \frac{1}{2} n^t \int g_V(E) P_i^t m^s(\mathbf{R}_i, E) e^{-2\kappa|\mathbf{R}_t-\mathbf{R}_i|} dE \quad (15)$$

However, since CC mode means constant *total* current, CC or CH simulations can be performed for the total profile, whereas only CH simulations can be performed for the normal and magnetic profiles separately. To obtain the CC profiles for the separated components, one can apply a separation procedure to the total CC profile, as done with the experimental STM data.

3.3.2. Application of atom superposition simulations to case of $Mn_3N_2(0\,1\,0)$

Atom superposition simulations have been made using Eq. (13) for the total profile using CC mode. The case of $Mn_3N_2(0\,1\,0)$ is an ideal system to simulate due to the fact that the spin vectors are aligned along the row directions and alternate by 180° from row to row; the situation is complicated by the existence of the two kinds of Mn sites, Mn1 and Mn2, which have different local bonding geometry. Consecutive Mn1 rows have anti-aligned magnetic moments, and the 2 Mn2 rows adjacent to any Mn1 row have their moments anti-aligned to that Mn1 row. Here we show results for the case of $Mn_3N_2(0\,1\,0)$ at $V_s = -0.2$ V.

To make comparison to the averaged experimental line profile, the sum in either Eq. (12) or Eq. (13) is evaluated over a two-dimensional set of Mn1 and Mn2 atoms corresponding to the respective surface atom sites. The corresponding corrugation map is projected onto the [0 0 1] direction (perpendicular direction to the [1 0 0] row direction), as indicated schematically in Fig. 5(a).

Values of the $n_\uparrow^{Mn1}$, $n_\downarrow^{Mn1}$, $n_\uparrow^{Mn2}$, and $n_\downarrow^{Mn2}$ are obtained from surface spin-polarized LDOS calculations, which were performed using density functional theory. A brief description and results of this approach for Mn_3N_2 will be given in Secion 3.3.3. The full results of these calculations for Mn_3N_2 will be published elsewhere. Values of the n^{Mn1}, m^{Mn1}, n^{Mn2}, and m^{Mn2} are calculated from the $n_\uparrow^{Mn1}$, $n_\downarrow^{Mn1}$, $n_\uparrow^{Mn2}$, and $n_\downarrow^{Mn2}$.

For simulation of the total profile using spin-↑ and spin-↓ LDOS values, the sum in Eq. (12) is evaluated by integrating the sample spin-polarized LDOS values from E_F to $E_F + eV_s$, obtaining the integrated LDOS (ILDOS) values $\tilde{n}_\uparrow^{Mn1}(V)$, $\tilde{n}_\downarrow^{Mn1}(V)$, $\tilde{n}_\uparrow^{Mn2}(V)$, $\tilde{n}_\downarrow^{Mn2}(V)$, which are plotted vs. V in Fig. 5(b).

For simulation of the total profile using normal and magnetic LDOS values, the sum in Eq. (13) is evaluated by integrating the sample n's and m's from E_F to $E_F + eV_s$ in order to obtain the ILDOS values $\tilde{n}^{Mn1}(V)$, $\tilde{m}^{Mn1}(V)$, $\tilde{n}^{Mn2}(V)$, and $\tilde{m}^{Mn2}(V)$, which are plotted vs. V in Fig. 5(c).

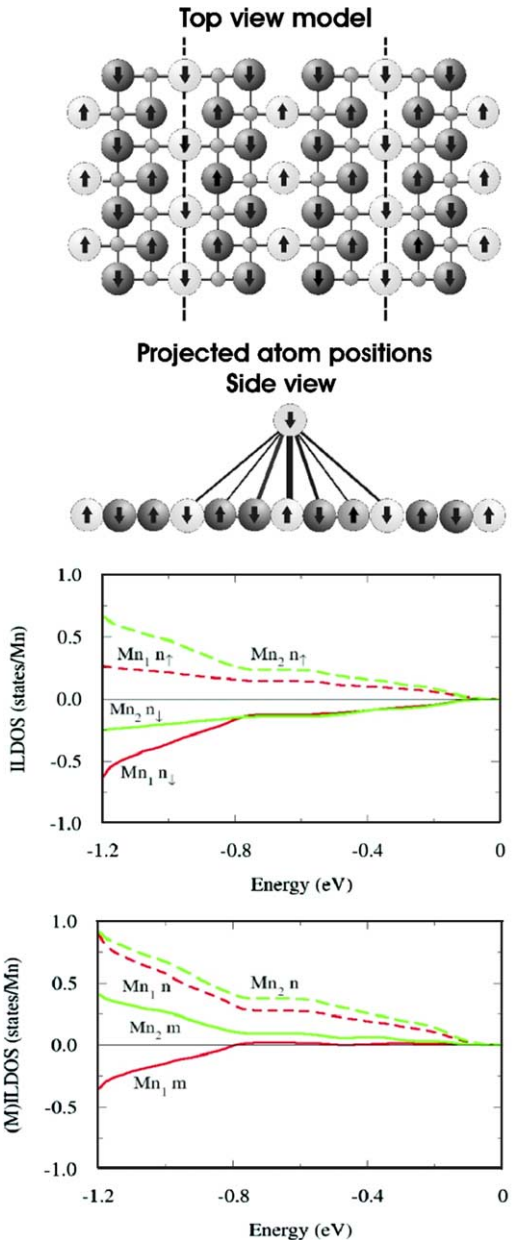

Fig. 5. (a) Illustration of the sample surface and tip-sample geometry. The side-view depicts the projected Mn positions onto the simulation line direction. Mn1 and Mn2 atoms are marked with light and dark colours correspondingly; vectors inside atoms represent the total magnetic moment of manganese atoms, which is layerwise aFM. Rows of Mn1 atoms having negative total magnetic moments are indicated with vertical dashed lines. (b) Majority and minority ILDOS values $\tilde{n}^{\mathrm{Mn1}}_{>}(\mathrm{V})$, $\tilde{n}^{\mathrm{Mn1}}_{<}(\mathrm{V})$, $\tilde{n}^{\mathrm{Mn2}}_{>}(\mathrm{V})$, $\tilde{n}^{\mathrm{Mn2}}_{<}(\mathrm{V})$. (c) Normal and magnetic ILDOS values $\tilde{n}^{\mathrm{Mn1}}(\mathrm{V})$, $\tilde{m}^{\mathrm{Mn1}}(\mathrm{V})$, $\tilde{n}^{\mathrm{Mn2}}(\mathrm{V})$, and $\tilde{m}^{\mathrm{Mn2}}(\mathrm{V})$.

Both methods (Eq. (12) or Eq. (13)) give equivalent results for the total line profile. Here we will show the result using Eq. (13) at energy $E = -0.2$ eV (energy relative to E_{F}), corresponding to the case of $V_{\mathrm{s}} = -0.2$ V. Values of normal and magnetic ILDOS for Mn1 and Mn2 were taken from the data of Fig. 5(c). Numerical values for the ILDOS used in the simulation are: $\tilde{n}^{\mathrm{Mn1}}(-0.2\ \mathrm{V}) = 0.104$, $\tilde{m}^{\mathrm{Mn1}}(-0.2\ \mathrm{V}) = 0.008$, $\tilde{n}^{\mathrm{Mn2}}(-0.2\ \mathrm{V}) = 0.138$, and $\tilde{m}^{\mathrm{Mn2}}(-0.2\ \mathrm{V}) = 0.029$ states/Mn. We note that over a window of energy on the negative side from 0 eV to $\sim$−0.8 eV (relative to E_{F}), the integrated majority LDOS is spin-↑ for both Mn1 and Mn2 (i.e. $\tilde{m}^{\mathrm{Mn1}}(-0.2\ \mathrm{V})$ and $\tilde{m}^{\mathrm{Mn2}}(-0.2\ \mathrm{V})$ are both positive). This means that the ordering of partial moments (magnetic integrated LDOS) within this energy window is actually ↑↑↑↓↓↓. It is important to note that this does not imply a magnetic reconstruction; the total magnetic moments still order as ↑↓↑↓↑↓.

For energies more negative than $\sim$−0.8 eV (relative to E_{F}), the integrated majority LDOS for Mn1 becomes spin-↓ while that for Mn2 remains spin-↑, which is evident from Fig. 5(c). For such larger negative energies, the ordering of partial moments (magnetic integrated LDOS) coincides with the ordering of the total magnetic moments which are ↑↓↑↓↑↓.

Shown in Fig. 6(a) is the total line profile simulation result using Eq. (13) with $P_i^{\mathrm{t}} = 10\%$, $\kappa = 1.1\ \mathrm{\AA}^{-1}$ and average tip-sample separation $\bar{z}_{\mathrm{t}}(-0.2\ \mathrm{V}) = 5\ \mathrm{\AA}$. The simulation clearly does not agree very well with the SP-STM line profile shown in Fig. 3(b). It does show the existence of reflection symmetry about a plane containing Mn1 atoms; however, rather than a modulation of the peak heights, the simulation shows a modulation of the valleys only.

Shown in Fig. 6(b) are the CC magnetic and non-magnetic line profiles extracted from the total CC line profile of Fig. 6(a) for $V_{\mathrm{s}} = -0.2$ V. We have also performed the simulations in Eqs. (14) and (15) using CH mode, with very similar results. As seen in Fig. 6(b), the magnetic and non-magnetic profiles both agree qualitatively well with the experimental profiles shown in Fig. 3(c). For the non-magnetic component, a simple sinusoid-like profile is obtained with period $\frac{c}{2}$, and for the

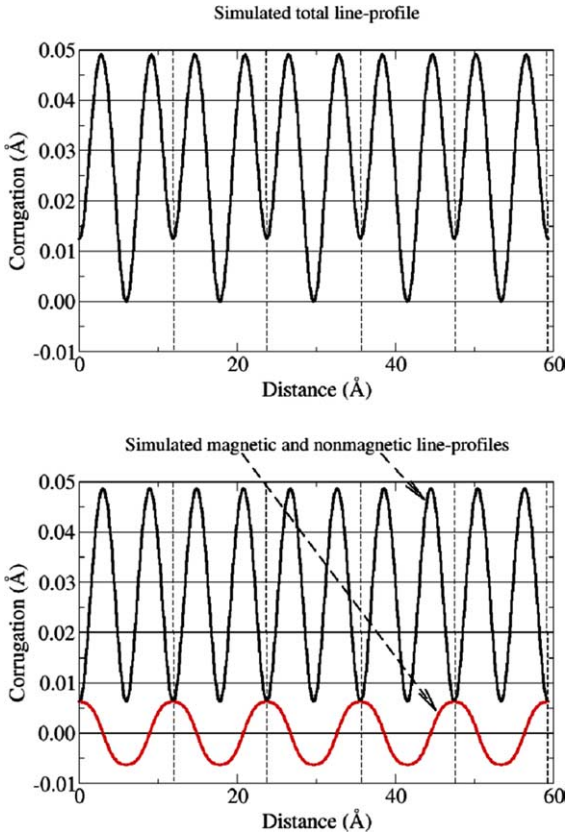

Fig. 6. (a) Simulated CC line profile calculated according to Eq. (13) for the case of $V_s = -0.2$ V with effective tip polarization 10% and average tip-sample separation 5 Å. (b) Simulated magnetic and non-magnetic line profiles extracted from total line profile. Vertical dashed lines indicate rows of Mn1 atoms with positive (M)ILDOS at −0.2 eV but with negative total magnetic moments.

magnetic component, a similar sinusoid-like profile is obtained with period c. We note that a more trapezoidal magnetic profile was obtained for the STM data shown in Fig. 4(c). Such a shape can also be simulated by varying the tip-sample separation slightly. However, as can be seen in Fig. 6(b), the peak position of the non-magnetic component is at the midpoint between two 2 Mn1 rows, whereas the peak position of the magnetic component in the simulation is at the Mn1 row. This is due to the non-magnetic ILDOS for Mn2 being larger than that of Mn1 at the surface (i.e. $\tilde{n}^{\mathrm{Mn2}}(-0.2\ \mathrm{V}) = 0.138 > \tilde{n}^{\mathrm{Mn1}}(-0.2\ \mathrm{V}) = 0.104$). Because of this, the total simulated profile does not resemble the total experimental profile. In this case, we modeled the tip as being ideal with tip LDOS centroid at the same position as the tip magnetic LDOS centroid.

As we have noted previously [21], these atom superposition corrugations underestimate the experimentally measured corrugations significantly, as is well known [26,29]. This is clearly the case for the result of Fig. 6, where the total simulated atom superposition corrugation is only ~0.05 Å, whereas the experimental total corrugation in Fig. 3(b) is ~0.14 Å and in Fig. 4(b) is ~0.28 Å. As shall be shown below, the full T–H simulations give much better agreement with the experimental STM corrugations, after tip broadening.

It should be emphasized that the ILDOS presented here in Fig. 5 and the resulting atom superposition simulations presented in Fig. 6 are based upon the results from surface ILDOS calculations, whereas in our previous 2 papers we made use of the ILDOS values from bulk calculations [8,21]. In fact the ILDOS values are very similar to those from bulk calculations, with some small differences, for example in the bulk calculations the ILDOS(Mn1) > ILDOS(Mn2), but for the surface calculations the ILDOS(Mn2) > ILDOS(Mn1), over the range from 0 to −0.8 eV. Although in either case the ILDOS of Mn1 and Mn2 are very similar, yet using the bulk values one finds the non-magnetic atom superposition line profile peaking on Mn1 as we showed in our earlier papers [8,21], whereas using surface values it peaks at the interstitial line between the 2 Mn2 atoms. It is clear however, from the non-magnetic atomic-resolution images [21], that the non-magnetic line profile peak does occur at the Mn1 position. It thus suggests the need to go beyond the atom superposition simulation method.

3.3.3. Simulations using Tersoff–Hamman method

While the method described above allows a very direct interpretation of the STM data and requires only the calculation of the ILDOS it is based on rather severe approximations. Therefore, in order to check the accuracy of the above approach we have performed in a next step an explicit

calculation of the surface density of states and applied the Tersoff–Hamann method to simulate the STM data. As in Section 3.2.1, we start with the spin-generalized Tersoff–Hamannn (TH) model (Eq. (1)). Assuming the magnetic and non-magnetic LDOS of the tip to be energy independent we get the following expression for the total tunnel current:

$$I_t \sim \int \mathrm{d}E g_V(E)[n^s(\{\mathbf{R}_t\},E) + P^t m^s(\{\mathbf{R}_t\},E)]. \tag{16}$$

As before, $P^t = \frac{m^t}{n^t}\cos\theta$ is the effective spin polarization of the tip. $n^s(\{\mathbf{R}_t\},E)$ and $m^s(\{\mathbf{R}_t\},E)$ are the surface non-magnetic and magnetic density of states at the position of the tip and at energy E. In order to evaluate these quantities we have performed an explicit calculation of the $Mn_3N_2(0\,1\,0)$ surface. We have employed density functional theory within the spin-LDA approximation [30]. Specifically, a plane-wave pseudo-potential approach as implemented in SFHIngX has been used [31]. Mn and N have been represented by Troullier–Martins pseudo-potentials with 3d, 4s, 4p (Mn) and 2s, 2p (N) states as valence. A plane-wave energy cutoff of 45 Ry and a $3\times3\times1(3\times3\times3)$ Monkhorst-Pack mesh for slab(bulk) have been found to give converged results with respect to surface energies, basis set and k-point sampling.

The surface has been modeled by a repeated slab geometry where each slab consists of 3 atomic layers with non-relaxed bulk geometry. The surface unit cell is that of the magnetic structure, i.e, each atomic layer contains 6 Mn and 4 N atoms. The slabs have been separated by a vacuum region of 9 Å. Convergence checks showed the chosen slab and vacuum thickness to give error bars in the surface energy of less then 2 meV/Å^2. Because the slab is only 3 layers thick, Mn1 surface atoms on either side of the slab can have significant direct interactions between them because there are no other atoms in between. Since the discrepancies between ILDOS summation models and direct T–H simulations to be discussed depend strongly on the nature of the surface states, some of the discrepancies may be artifacts of the too small slab thickness. Despite converged surface energies, an accurate reproduction of previously published non-magnetic bias dependent Mn_3N_2 (0 1 0) STM data from Ref. [21] has not been achieved. While in experiment at almost all bias voltages both Mn1 and Mn2 atoms can be recognized, in our T–H simulations Mn1 atoms become visible only at tip-surface distances less than 2.5 Å. Also, the experimental trend that the Mn2 corrugation contrast becomes more pronounced with increasing bias magnitude is only poorly reproduced. Although these trends could apparently be reasonably well described in the ILDOS model [21], the T–H simulations here show that one should be rather cautious about this previous success, because the T–H simulations show that the fully spatially resolved spin densities on the surface show a strong directionality which is missed by the atom-lumped spherically averaged ILDOS model.

We attribute these deficiencies to the slab thickness which is not sufficient to accurately reproduce the lateral corrugation. However, as shown in next section, it provides reasonable results for the averaged corrugation values.

An inspection of the local density of states as obtained in the plane-wave basis showed that beyond a distance of ≈3 Å from the surface, the density becomes exceedingly noisy. While this behavior has no effect on physical entities such as lattice constants or surface energies, it makes STM simulations for tip-surface separations larger than ≈3 Å unreliable. To overcome this problem we have projected our wavefunctions $\Psi_{i,k}$ from the plane wave basis onto a basis set of atomic orbitals μ:

$$|\Psi_{i,k}\rangle = \sum_{\mu} |\mu\rangle\langle\mu|\Psi_{i,k}\rangle \tag{17}$$

$$\langle\mu|\Psi_{i,k}\rangle = \sum_{G} \langle\mu|G+k\rangle\langle G+k|\Psi_{i,k}\rangle \tag{18}$$

As atomic orbitals, the manganese s, d atomic pseudo-wavefunctions have been used. To test the completeness of the atomic basis set, the above projection procedure has been checked comparing results of SP-STM simulations at short tip-sample distances (<3 Å) for both basis set types. In all cases, the effect on corrugation profiles for total,

magnetic and non-magnetic components has been found to be not significant. Therefore, for tip-sample distances >3 Å, the above projection method has been used.

3.3.4. Application of Tersoff–Hamann method

Based on the above described method, we have calculated the surface LDOS. Fig. 7(a) shows the averaged corrugation profile of a CC simulation at bias voltage $V_s = -0.2$ V. The simulations have been performed for an average tip-surface separation of 5 Å and for an effective tip polarization $P^t = 90\%$. The magnetic and non-magnetic profiles from the same calculation are shown in Fig. 7(b).

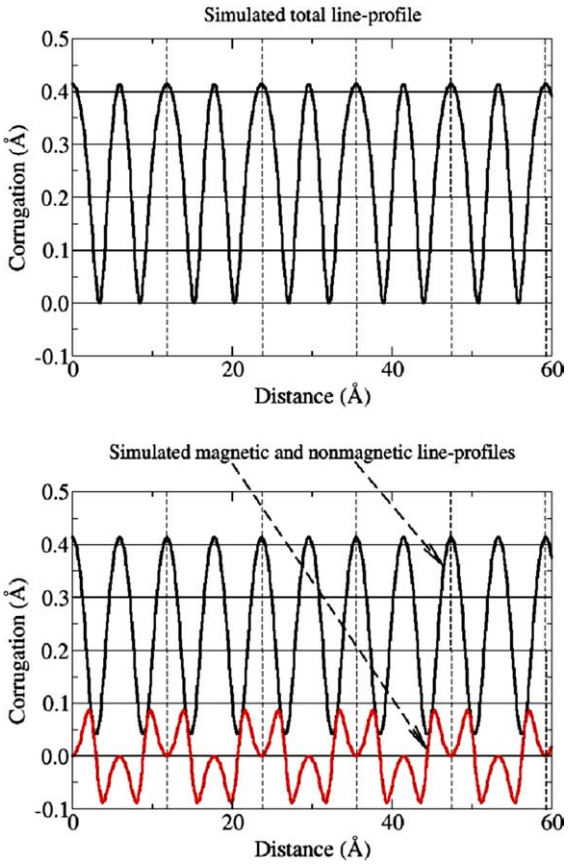

Fig. 7. (a) Simulated CC line profile calculated according to Eq. (16) for the case of $V_s = -0.2$ V with effective tip polarization 90% and average tip-sample separation 5 Å. (b) Simulated magnetic and non-magnetic line profiles extracted from total profile. Vertical dashed lines indicate rows of Mn1 atoms with positive (M)ILDOS at −0.2 eV but with negative total magnetic moments. Note the different scales in this figure and in Fig. 6.

A comparison with the magnetic and non-magnetic profile as calculated within the ILDOS atom superposition schema [Fig. 6(b)] shows clear differences. Using the latter method, for the non-magnetic part the corrugation amplitude is underestimated by a factor of ≈7 and the phase is shifted by $c/4$, i.e., by one quarter of the size of the magnetic surface unit cell. Thus, whereas surface ILDOS atom superposition finds a maximum at midpoint between Mn1, the full surface calculation finds the maximum at Mn1. Thus, the TH method finds better agreement with the separate magnetic and non-magnetic profiles.

For the magnetic part, the ILDOS and TH profile both show the same periodicity which is twice that of the non-magnetic corrugation. An interesting difference is that TH clearly resolves each row of Mn atoms while the ILDOS atom superposition-based results superimpose a Mn1 and the two surrounding Mn2 rows together. In order to analyze the origin for this discrepancy, we have studied in detail the spatially resolved spin-LDOS. Fig. 8 shows a cross-section through the surface along the [0 0 1] axis (b) and [1 0 0] axes (c) and (d) for a bias voltage $V_s = -0.2$ V. For the following discussion let us focus on the Mn1 which is shown in Fig. 8(a) and which is the center atom in Fig. 8(b) and (c). From the ILDOS—which integrates the spin-density over a sphere around the Mn1 nucleus—this atom is found to have an integrated spin-up moment (positive m) at the considered bias. The dominance of the spin-up density can be nicely seen in Fig. 8(c). However, what can be also seen in this figure and in Fig. 8(b) is that in the region probed by the STM tip the spin-density is negative. Thus, in an STM image, and at this bias, this atom would appear to be spin down despite the fact that the ILDOS for this atom is spin up. The reason for the discrepancy between the ILDOS spherical atom superposition and the TH density of states is the appearance of strongly directed orbitals at the surface atoms. An analysis of these orbitals showed that they have mainly Mn sd character.

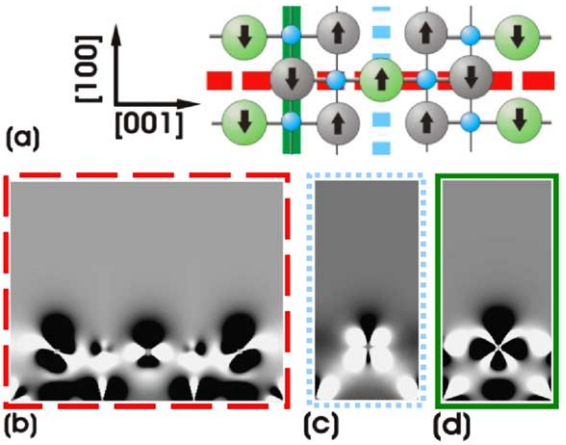

Fig. 8. (a) Schematic view of the atomic and magnetic structure of the top surface layer. The arrows inside the atoms indicate the sign of the magnetic moment as determined by ILDOS at bias voltage $V_s = -0.2$ V, i.e. by integrating corresponding LDOS over a sphere around each atom and over energy. (b)–(d) show contour plots of the magnetic LDOS for the case of $V_s = -0.2$ V where bright and dark regions correspond to spin-up and spin-down densities correspondingly. The contour plots shown are the cross-sections through the surface layer along [0 0 1] axis (b) and the [1 0 0] axis (c, d). Horizontal and vertical bars of (a) show cross-section position of (b)–(d) correspondingly. (for a colour version of the figure see the online paper.)

Thus in Fig. 7, the Mn1 with positive (M)ILDOS at −0.2 eV (at dashed lines) appears as a valley. From Fig. 8(b), 2 additional negative spin lobes are seen which are for the Mn2 atoms with negative (M)ILDOS at −0.2 eV—these appear as the negative going peaks in Fig. 7(b). Because of the aFM symmetry, the Mn2 atoms with positive (M)ILDOS at −0.2 eV [not shown in Fig. 8(b)] will have positive spin lobes and therefore appear as the positive-going peaks in Fig. 7(b). Likewise, the Mn1 atoms with negative (M)ILDOS at −0.2 eV also have positive spin lobes and thus appear as the valley between the negative-going Mn2 peaks.

As discussed in connection with the lateral shift between magnetic and non-magnetic profiles in case of the Mn-coated tip (Fig. 3) there is strong evidence that the tip consists of several apex atoms. We have therefore also performed the above simulations assuming a STM tip that has more than one atom in the apex. Specifically, we assumed a tip apex consisting of four non-interacting s-like atoms sitting in the corners of a square. All four atoms lie in a plane parallel to the surface and each atom contributes to the total tunneling current according to the Tersoff–Hamann picture. Corrugation profiles for such a tip are shown in Fig. 9. As expected, the 4-atom-tip averages the corrugation profiles when compared with those obtained from a single-atom tip. The amplitude of the corrugation significantly decreases with increasing tip area and comes close to that observed in experiment (see Figs. 3 and 4). It is also interesting to note that the exact geometry

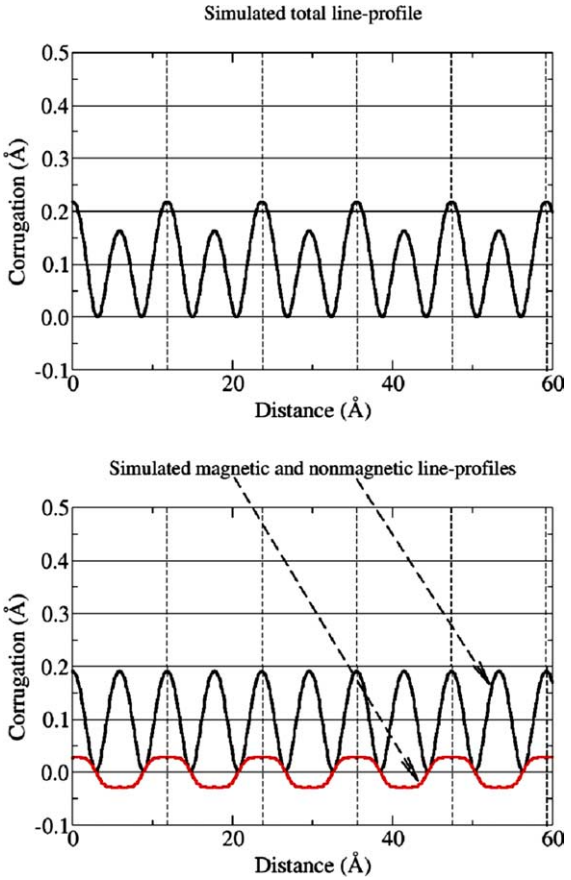

Fig. 9. (a) Simulated CC line profile calculated according to Eq. (16) for the case of $V_s = -0.2$ V with effective tip polarization 90%, average tip-sample separation 5 Å, and a tip consisting of four apex atoms with lateral atom–atom distance 1.9 Å. (b) Simulated magnetic and non-magnetic line profiles extracted from the total profile. Vertical dashed lines indicate rows of Mn1 atoms with positive (M)ILDOS at −0.2 eV but with negative total magnetic moments.

of the tip changes the shape of the corrugation: for a lateral apex atom-to-atom distance of 1.9 Å, a trapezoidal shape is found, while for a distance of 2.1 Å, a sinusoidal shape is observed.

An interesting trend observed when going to larger tip-surface distances is that the calculated T–H magnetic profile gets closer and closer to the one observed experimentally. However, our present calculations allow a maximum tip-surface distance of only up to 5.5 Å where still differences between theory and experiment can be seen. Based on these trends we estimate for a tip-surface separation of 7–8 Å even for a single-atom tip a magnetic profile that closely matches experiment. In any case, our simulations (including those based on bulk and surface LDOS, and atom superposition and T–H) are all in agreement that at −0.2 eV we should observe the spin ordering as ↑↑↑↓↓↓, which agrees with the experimental observation.

4. Conclusions

SP-STM has become a powerful technique for resolving spin structures on an atomic scale. We have presented new SP-STM data acquired using magnetic-coated probe tips on $Mn_3N_2(0\,1\,0)$. We have shown firstly that the magnetic state of the tip can change during scanning, which is attributed to structural changes of the tip involving a small number of atoms at the apex of the tip. Local rearrangements of the tip atoms can produce spin-polarized and non-spin-polarized STM images of the same local area of a surface. We have shown that tips coated with aFM materials (Mn and MnN) can obtain atomic-scale magnetic modulation on aFM surfaces as well as tips coated with FM materials (Fe). SP-STM images in the vicinity of step edges prove that the surface magnetic structure corresponds directly to that of the bulk magnetic structure of Mn_3N_2. The SP-STM tunneling current is written in terms of spin-↑ and spin-↓ channels, which can be re-written in terms of non-magnetic and magnetic ILDOS. From this it is possible to make simulations of both the magnetic and non-magnetic components. Simulations in CC mode are performed for the total current and then resolved into components using a separation procedure. A comparison of simulations based on atom superposition vs. full Tersoff–Hamann show that, although atom superposition has some success, in general the full T–H approach is required to simulate the data in SP-STM. This is due largely to the details of the specific spin-resolved surface states which have highly directional character. However, while the full DFT calculations find qualitatively good agreement with both the magnetic and non-magnetic profiles, tip broadening in the form of multiple tip atoms is found to give improved agreement with the experimental line profiles.

Acknowledgements

This work is supported by the National Science Foundation under grant Nos. DMR-9983816 and DMR-0304314. H.Q. Yang also thanks the Ohio University Post-doctoral Fellowship program for support. The work at CWRU was funded by the Office of Naval Research under grant number N00014-02-1-0880.

References

[1] J. Tersoff, D.R. Hamann, Phys. Rev. Lett. 50 (25) (1983) 1998;
J. Tersoff, D.R. Hamann, Phys. Rev. B 31 (1985) 805.
[2] J. Stroscio, R. Feenstra, A. Fein, Phys. Rev. Lett. 57 (1986) 2579.
[3] R. Feenstra, J. Stroscio, A. Fein, Surf. Sci. 181 (1987) 295.
[4] D. Biegelsen, R. Bringans, J. Northrup, L. Swartz, Phys. Rev. B 41 (1990) 5701.
[5] K.W. Haberern, M.D. Pashley, Phys. Rev. B 41 (1990) 3226.
[6] P. Mutombo, V. Cháb, Surf. Sci. 532 (2003) 645.
[7] S. Heinze, M. Bode, A. Kubetzka, O. Pietzsch, X. Nie, S. Blügel, R. Wiesendanger, Science 288 (2000) 1805.
[8] H.Q. Yang, A.R. Smith, M. Prikhodko, Walter R.L. Lambrecht, Phys. Rev. Lett. 89 (2002) 226101.
[9] R. Wiesendanger et al., Phys. Rev. Lett. 65 (1990) 247.
[10] D. Wortmann, S. Heinze, Ph. Kurz, G. Bihlmayer, S. Blügel, Phys. Rev. Lett. 86 (2001) 4132.
[11] M. Bode, S. Heinze, A. Kubetzka, O. Pietzsch, M. Hennefarth, M. Getzlaff, R. Wiesendanger, X. Nie, G. Bihlmayer, S. Blügel, Phys. Rev. B 66 (2002) 014425.
[12] H.Q. Yang, H. Al-Brithen, A.R. Smith, J.A. Borchers, R.L. Cappelletti, M.D. Vaudin, Appl. Phys. Lett. 78 (2001) 3860.

[13] H.Q. Yang, H. Al-Brithen, A.R. Smith, E. Trifan, D.C. Ingram, J. Appl. Phys. 91 (2002) 1053.
[14] M. Tabuchi, M. Takahashi, F. Kanamaru, J. Alloys Compd. 210 (1–2) (1994) 143.
[15] K. Suzuki et al., J. Alloys Compd. 306 (2000) 66.
[16] A. Leineweber, R. Niewa, H. Jacobs, W. Kockelmann, J. Mater. Chem. 10 (12) (2000) 2827.
[17] D.H. Martin, Magnetism in Solids, Iliffe Books Ltd., London, 1967, p. 67.
[18] A.M. Keen, S.H. Baker, C. Binns, S.N. Mozley, C. Norris, H.S. Derbyshire, Solid State Commun. 107 (1998) 523.
[19] G. Kreiner, H. Jacobs, J. Alloys Compd. 183 (1992) 345.
[20] H. Jacobs, C. Stuve, J. Less Common Metals 96 (1984) 323.
[21] H.Q. Yang, R. Yang, A.R. Smith, W.R.L. Lambrecht, Surf. Sci. 548 (2004) 117.
[22] A.J. Heinrich, C.P. Lutz, J.A. Gupta, D.M. Eigler, Science 298 (2002) 1381.
[23] S.W. Hla, K.F. Braun, K.H. Rieder, Phys. Rev. B 67 (2003) 201402.
[24] T.M. Wallis, N. Nilius, W. Ho, Phys. Rev. Lett. 89 (2002) 236802.
[25] T.K. Yamada, M.M.J. Bischoff, T. Mizoguchi, H. van Kempen, Appl. Phys. Lett. 82 (9) (2003) 1437.
[26] C.J. Chen, Introduction to Scanning Tunneling Microscopy, Oxford University Press, 1993.
[27] A. Kubetzka, M. Bode, O. Pietzsch, R. Wiesendanger, Phys. Rev. Lett. 88 (5) (2002) 057201.
[28] R.M. Tromp, R.J. Hamers, J.E. Demuth, Phys. Rev. B 34 (1986) 1388.
[29] S. Heinze, S. Blügel, R. Pascal, M. Bode, R. Wiesendanger, Phys. Rev. B 58 (24) (1998) 16432.
[30] J.P. Perdew, A. Zunger, Phys. Rev. B 23 (1981) 5048.
[31] See <http://www.sfhingx.de>.
[32] W.R.L. Lambrecht, M. Prikhodko, M.S. Miao, Phys. Rev. B 68 (2003) 174411.